Spin-wave quantum computing with atoms in a single-mode cavity

Kevin C. Cox [1,*], Przemyslaw Bienias [2], David H. Meyer [1], Donald P. Fahey [1],
Paul D. Kunz [1], and Alexey V. Gorshkov [2]

[1]*DEVCOM Army Research Laboratory, Adelphi, Maryland 20783, USA*
[2]*Joint Quantum Institute and Joint Center for Quantum Information and Computer Science,
NIST/University of Maryland, College Park, Maryland 20742, USA*

We present a method for network-capable quantum computing that relies on holographic spin-wave excitations stored collectively in ensembles of qubits. We construct an orthogonal basis of spin waves in a one-dimensional array and show that high-fidelity universal linear controllability can be achieved using only phase shifts, applied in both momentum and position space. Neither single-site addressability nor high single-qubit cooperativity is required, and the spin waves can be read out with high efficiency into a single cavity mode for quantum computing and networking applications. We describe how to establish linear quantum processing using a lambda scheme in a rubidium-atom system and calculate the expected experimental operational fidelities due to fundamental and technical errors. We derive efficient methods to achieve linear controllability in both a single-ensemble and dual-ensemble configuration. Finally, we propose to use the spin-wave processor for continuous-variable quantum information processing and present a scheme to generate large dual-rail cluster states useful for deterministic computing.

I. INTRODUCTION

Laser-cooled atoms in optical resonators are a building block for many of the most exquisite demonstrations of quantum electrodynamics. Atom-cavity systems are the basis for state-of-the-art quantum simulators [1,2], quantum memories [3], and entanglement-enhanced atomic clocks [4,5]. With atom number N commonly between 10^3 and 10^6, an ensemble's intrinsic capacity to store quantum information is enormous, with a state space of dimension 2^N. Designing quantum platforms that are able to access and process this large amount of quantum information is a grand challenge in atomic science. Here, we analyze a method to store quantum information as collective spin-wave excitations and realize universal quantum computation in a system where the spin waves may be efficiently retrieved into a single optical cavity mode.

Future quantum computers will likely be most useful when connected together into a quantum network, much like classical computers. Quantum processors based on atoms, ions, and superconducting qubits are advancing in their capability to perform high-fidelity operations within a single science chamber [6–8]. However, scaling up of these systems into a network or heterogeneous computer is still a serious challenge, since qubits must be coupled to an optical communication channel with high efficiency and fast demultiplexing. Spin-wave quantum processors may address this difficulty, by using quantum information stored as one-dimensional (1D) spin-wave holograms in an ensemble of qubits, which can exhibit collectively enhanced coupling to a single optical mode [9–11].

Recent experiments have introduced a path to use collective ground-state spin-wave excitations to achieve high-capacity quantum memories [11–15], but these experiments have not introduced a method to achieve full linear controllability of spin-wave excitations, a prerequisite for a universal quantum processor. Spin-wave quantum systems are being realized in multiple physical platforms including atomic vapors [11,13–15], solid-state crystals [16–18], and superconducting circuits [19]. Proposals for spin-wave readout of atomic arrays have also been developed [20–22]. However, demonstrating platforms that simultaneously achieve universal quantum processing, high capacity, and efficient optical readout is still an ongoing challenge.

First, in Secs. II and III, we describe the spin-wave computation basis in a one-dimensional lattice and discuss a physical apparatus consisting of two atomic ensembles coupled to a single optical cavity mode. In Sec. III A, we describe a set of operations that enable universal quantum computing within the ensemble memory, specifically discussing the implementation of *in situ* linear-optical quantum computing with spin waves. We first discuss a method using two distinct atomic ensembles inside a single cavity mode. Although the two-ensemble approach is experimentally attractive, in Sec. IV, we show that linear controllability can also be achieved in a single ensemble. In Sec. V, we evaluate the dominant fundamental and technical performance limitations of linear operations and

*Corresponding author: kevin.c.cox29.civ@army.mil

discuss initialization and readout. In Sec. VI, we present a proposal for deterministic continuous-variable quantum computing using spin-wave cluster states. We calculate that it may be possible to achieve a continuous-variable cluster state with thousands of modes and greater than 20 dB of squeezing per mode, a significant computational resource for deterministic continuous-variable processing [23–25]. We assert that our proposal may be realized using current experimental techniques, operating at performance levels already demonstrated in laboratory settings.

This paper builds upon a significant body of recent work in many-body cavity quantum electrodynamics [2,26–32] and memory experiments showing that quantum information can be stored as holographic spin waves in a large group of qubits [9–11,33–36] that can be transferred to a readout bus for retrieval [13,15,37,38]. Phase modulation of spin waves has been used to observe interference between two holographic profiles [39], but spatial phase shifts alone are not sufficient to create arbitrary linear unitary operations, a condition we refer to as linear controllability, which is required for universal quantum processing [40]. Additional related works have theoretically investigated quantum information processing with holographic spin waves in superconducting circuits [9] and discussed how to implement spin-wave beam splitters using modulation of transverse beams [35].

Much progress has been made, both experimentally and theoretically, using single ground-state atoms, Rydberg atoms, and Rydberg ensembles inside of optical cavities to realize quantum operations with enhanced readout [27,41–43]. This proposal is complementary to these previous works and may yield an easier route toward networkable scalability to hundreds of modes without the need to access Rydberg states.

Overall, spin-wave quantum information has a number of promising advantages. Hundreds of ground-state spin-wave excitations can be stored in a single ensemble [13]. Spin waves can be used in the single-photon regime or the continuous-variable regime that is amenable to powerful and efficient quantum error correction [44]. Data are stored in ground states with coherence times that can be driven up to the second timescale [45]. Spin waves have collectively enhanced qubit-light coupling that leads to efficient readout [11]. The primary advance of this work is to combine spatial phase gradients with cavity dressing to achieve linear controllability, and therefore universal quantum computing, with capacities of up to 1000 spin waves in a single cavity mode.

II. SETUP

The apparatus and atomic levels are diagrammed in Figs. 1(a) and 1(b). We first consider two ensembles, each with N laser-cooled alkali atoms, approximated as three-level atoms with long-lifetime states $|g\rangle$, $|e\rangle$ and optically excited state $|i\rangle$ with linewidth Γ. While we focus on laser-cooled atoms in this paper, the concepts of this proposal may be easily modified for use with a variety of ensemble quantum memory platforms. The atoms are confined in two 1D periodic potentials, each with M sites, inside of a running-wave optical cavity. The two arrays, labeled "A" and "B," have the same cavity couplings and experimental parameters. When discussing parameters
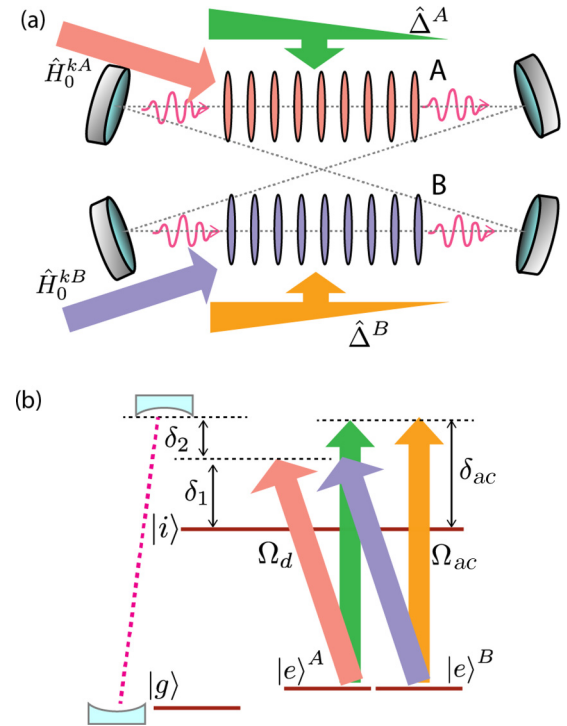
FIG. 1. Setup and level diagram using alkali atoms. (a) Two ensembles are coupled to a single running-wave cavity, and operations are applied using potential gradients (green and orange) with operators $\hat{\Delta}^A$ and $\hat{\Delta}^B$ and Raman dressing beams (red and violet) with associated Hamiltonians $\hat{H}_0^{kA}$ and $\hat{H}_0^{kB}$. (b) Level diagram. Raman cavity coupling is controlled with the dressing beams (red and violet). Optical gradients are applied with large detuning δ_{ac}. The $|e\rangle$ states in ensembles A and B are drawn separately to delineate the ensemble-specific beams.

and operators that specifically refer to one array or the other, we will denote them with a corresponding superscript A or B.

A running-wave cavity is required for this experiment in order to distinguish between excitations with left- or right-traveling photons. The arrays are optically interrogated using Raman dressing beams (red and violet in Fig. 1) that stimulate two-photon Raman transitions. Potential gradients (green and orange in Fig. 1), using laser beams with an intensity variation, are applied perpendicular to the cavity axis. The off-resonant optical fields are applied with detuning δ_{ac} and a spatially varying Rabi frequency $\Omega_{ac}(x)$.

The optical cavity is described by its finesse f, full-width-at-half-maximum (FWHM) linewidth κ, Jaynes-Cummings coupling parameter g associated with the $|g\rangle$-to-$|i\rangle$ transition, and single-atom cooperativity parameter $C = 4g^2/\kappa\Gamma$. We consider an apparatus with C near or less than 1, but large collective cooperativity $NC \gg 1$. Atoms in $|e\rangle$ can be made to interact with the cavity mode by applying Raman dressing lasers (red and violet in Fig. 1) with Rabi frequency Ω_d. The Raman dressing lasers are detuned from the $|g\rangle$-to-$|i\rangle$ transition by a frequency δ_1. The cavity is tuned near a two-photon resonance with the Raman dressing lasers with a two-photon detuning of δ_2.
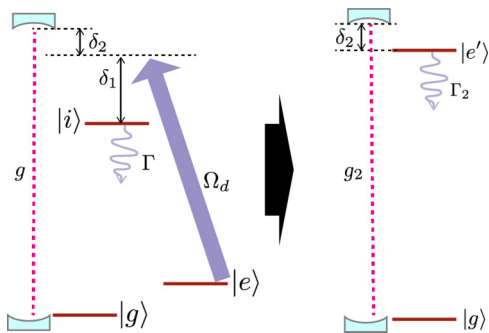
FIG. 2. Three-level diagram and adiabatic elimination. The experimental three-level system is treated as a dynamic two-level system with cavity coupling rate g_2, excited state lifetime Γ_2, and atom-cavity detuning δ_2.

With large detuning δ_1 ($|\delta_1| \gg |\delta_2|$, $\sqrt{N}g$, Ω_d) between the cavity and the $|g\rangle$-to-$|i\rangle$ transition, the theoretical treatment of Fig. 1(a) may be simplified by adiabatically eliminating $|i\rangle$, creating an effective two-level system (Fig. 2) with dressed excited state $|e'\rangle$ and two-photon scattering rate

$$\Gamma_2(t) = \Gamma \frac{\Omega_d^2(t)}{4\delta_1^2}, \tag{1}$$

where $\Omega_d(t)$ is the Rabi frequency of the Raman dressing laser. This results in a new two-photon Jaynes-Cummings coupling parameter

$$g_2(t) = \frac{g\Omega_d(t)}{2\delta_1}. \tag{2}$$

In addition to the two-photon transition rates, the Raman dressing laser gives rise to shifts in the cavity resonance frequency and the two-photon transition frequency that must be taken into account (see Sec. V E).

A diagram that defines the experimental parameters and the relationship between the three-level system and the two-level model is shown in Fig. 2. There are several important advantages of this three-level scheme. Critically, the effective cavity coupling $g_2(t)$ and free-space scattering rate $\Gamma_2(t)$ are dynamic and may be turned on and off at high speed via the dressing laser intensity, proportional to $|\Omega_d(t)|^2$.

III. MOMENTUM BASIS WITH ALKALI ATOMS IN CAVITY

We demonstrate linear controllability by defining a set of orthogonal spin-wave modes in the momentum basis. We first discuss how this proposal may be realized in a three-level Raman system with two ensembles of laser-cooled and trapped alkali atoms inside a single optical cavity mode. Then, in Sec. IV, we show how to extend the proposal to using only a single ensemble. Using cold atoms, two arrays may be created via counterpropagating trap beams within the cavity, or the single sites may be created by projecting an additional trapping potential transverse to the cavity mode. The latter scheme may be useful to precisely control the trap dimension and spacing of the array sites.
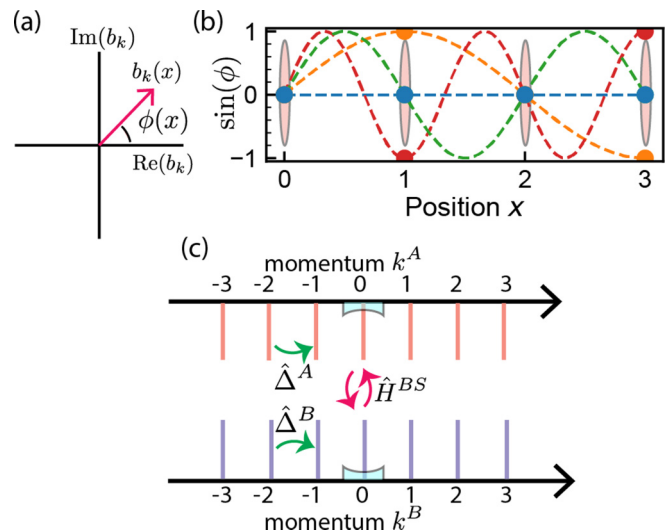
FIG. 3. Momentum basis. (a) Spin-wave eigenstates are characterized by an excitation amplitude $b_k(x)$ with spatially dependent phase $\phi(x)$, $b_k(x) = \frac{1}{\sqrt{M}}e^{i\phi(x)} = \langle ggg\cdots|\,\hat{a}_x\hat{b}_k^\dagger\,|ggg\cdots\rangle$. (b) Momentum eigenstates with $M = 4$ sites, labeled by momentum number k ranging from $k = 0$ to $k = 3$ (blue, orange, green, and red, respectively). Dashed lines are guides for the eye, with physical phases represented by solid points. (c) Connectivity diagram. The momentum shifts $\hat{\Delta}$ and cavity beam splitter $\hat{H}^{BS}$ allow full connectivity for spin waves. k is defined modulo M so that $k = -1$ is equivalent to $k = M - 1$.

In general, the lowering operator that describes a collective excitation at array site x is defined as

$$\hat{a}_x = \frac{1}{\sqrt{n}} \sum_{l=0}^{n-1} |g_l\rangle\langle e_l|, \tag{3}$$

where we sum over all atoms l at site x and $|g_l\rangle$ and $|e_l\rangle$ are the ground and excited states of the two-level atoms.

In this paper, we are interested in the corresponding momentum states, where excitations are stored in an equal superposition of all the lattice sites, with spatially dependent phase. The orthogonal set of momentum operators are defined over the full set of M array sites:

$$\hat{b}_k = \frac{1}{\sqrt{M}} \sum_{x=0}^{M-1} e^{i2\pi xk/M} \hat{a}_x. \tag{4}$$

The integer index $0 \leqslant k \leqslant M - 1$ delineates the orthogonal basis of momentum operators. The zero-momentum excitations, created by the $\hat{b}_0^\dagger$ operator acting on the ground state $|ggg\cdots\rangle$, are simply an equal superposition of all atoms, with common phase (see Fig. 3). Working with (including initializing and reading out) excitations in the $\hat{b}_k$ modes is experimentally advantageous because it relaxes the requirement for single-site addressability while retaining the full M-mode Hilbert space. We will show that any mode $\hat{b}_k$ can be efficiently read out into the cavity mode by using a momentum shift operation.

If the number of excitations at every site is small compared with n, $\hat{b}_k$ is equivalent to a canonical photon-lowering operator in mode k by the Holstein-Primakoff approximation [46].

In this paper, we assume this approximation to be valid. Spin-wave computing is also likely to be possible outside of the linear regime, but this is beyond the scope of this initial work. As such, the spin-wave operators $\hat{b}_k$ define a set of M independent bosonic modes, analogous to M optical channels. Unlike an optical system, the spin-wave excitations are stationary, stored as patterns in the large ensemble of atoms. We show that linear optical quantum computing may be performed in this M-mode system by describing how to perform arbitrary linear unitary operations.

A. Operations

The Raman dressing interrogation beams (red and violet) and ac Stark shift gradient beams (green and orange) shown in Fig. 1 define two Hamiltonians that may be applied to either ensemble A or ensemble B (denoted by superscripts when necessary). In this section, we present these Hamiltonians and discuss how they lead to linear controllability.

First, the ac Stark shift gradient Hamiltonian in the Raman system is

$$\hat{H}_\Delta = \sum_{x=0}^{M-1} \frac{\hbar\Omega_{\mathrm{ac}}^2(x)}{4\delta_{\mathrm{ac}}} \hat{a}_x^\dagger \hat{a}_x. \tag{5}$$

With a choice of $\Omega_{\mathrm{ac}}^2(x) \propto x$, this Hamiltonian allows arbitrary shifts in momentum k^A and k^B and has a corresponding unitary that we denote $\hat{\Delta}$:

$$\hat{\Delta} = \sum_{x=0}^{M-1} \left[\sum_{l=1}^{n} (|g_l\rangle\langle g_l| + e^{2\pi i x/M}|e_l\rangle\langle e_l|) \right]. \tag{6}$$

The behavior of $\hat{\Delta}$ is similar to other gradient quantum memories using collective ensembles [47,48].

In this proposal, atom-cavity interactions are governed by the Raman dressing lasers. We assume that $|\delta_2| \gg \Omega_2$, so that the collective atom-cavity interaction is dispersive, with Hamiltonian

$$\hat{H}_0^k = -\frac{\hbar\Omega_2^2}{4\delta_2} \hat{b}_0^\dagger \hat{b}_0, \tag{7}$$

where Ω_2 and δ_2 are the effective coupling strength and detuning for the two-photon transition [Eq. (2)]. The atom-cavity Hamiltonian [Eq. (7)] is derived in the Appendix.

When the Raman dressing lasers, with Rabi frequencies Ω_2^A and Ω_2^B, are applied simultaneously to ensemble A and ensemble B, a spin-wave beam-splitter Hamiltonian results,

$$\hat{H}^{\mathrm{BS}} = -\frac{\hbar\Omega_2^2}{4\delta_2} (\hat{b}_0^{\dagger A} + \hat{b}_0^{\dagger B})(\hat{b}_0^A + \hat{b}_0^B)$$

$$= a\begin{pmatrix} 1 & 1 \\ 1 & 1 \end{pmatrix}, \tag{8}$$

for $a \equiv -\hbar\Omega_2^2/(4\delta_2)$, where the second line has been written in the $(|b_0^A\rangle, |b_0^B\rangle)$ basis. $\hat{H}^{\mathrm{BS}}$ can be verified as a beam-splitter Hamiltonian by again calculating the unitary evolution $\hat{\Pi} = e^{-i\hat{H}^{\mathrm{BS}}t/\hbar}$, which can be written as

$$\hat{\Pi} = \frac{1}{2}\begin{pmatrix} 1 + 1e^{-2ita} & -1 + 1e^{-2ita} \\ -1 + 1e^{-2ita} & 1 + 1e^{-2ita} \end{pmatrix}. \tag{9}$$

B. Linear optical quantum computing

Most importantly, the two-mode beam splitters H^{BS}, in combination with the momentum displacement operators $\hat{\Delta}$ and spin-wave phase shifts $\hat{H}_0^k$, create a fully connected graph of spin-wave modes [Fig. 3(c)], sufficient for linear controllability in the register of $2M$ modes [40]. This construction of efficient linear controllability is one of the key results of this work, since linear controllability and memory readout are precisely the two requirements for universal linear optical quantum computing [49]. This approach has a further advantage experimentally in that any of the M^2 possible beam splitters may be accomplished in constant (independent of M) time, although there is a disadvantage that multiple beam splitters cannot be run in parallel. Next, we discuss a general proof of linear controllability that does not require two separate ensembles and discuss alternative beam-splitter constructions.

IV. QUANTUM PROCESSING WITH ONE ENSEMBLE

A. Controllability proof

So far in this paper, we have focused on using two atomic ensembles and performing beam splitters between spin waves in each. This is a simple experimental realization, but it is not fundamentally necessary for linear controllability. We now present a general proof that phase shifts alone are sufficient for controllability, even with one ensemble. For the general proof, we allow ourselves to utilize Hamiltonian generators $|a_x\rangle\langle a_x|$, with $x = 0, \ldots, M-1$, and $|b_0\rangle\langle b_0|$, where $|a_x\rangle = \hat{a}_x^\dagger|ggg\cdots\rangle$ and $|b_0\rangle = \hat{b}_0^\dagger|ggg\cdots\rangle$. These generators correspond to the applications of phase shifts in position space and momentum space.

A necessary and sufficient condition for controllability on the underlying M-dimensional Hilbert space is that our $M+1$ Hamiltonian terms generate the (M^2-1)-dimensional Lie algebra su(M) [50,51]. Working in the $|a_x\rangle$ basis, we first construct all the $M-1$ diagonal generators by taking linear combinations of $|a_x\rangle\langle a_x|$. We construct half [i.e., $M(M-1)/2$] of all the off-diagonal generators by considering, for $j \neq l$,

$$[[|b_0\rangle\langle b_0|, |a_j\rangle\langle a_j|], |a_l\rangle\langle a_l|]$$

$$\propto \frac{1}{\sqrt{M}}[|b_0\rangle\langle a_l| - |a_l\rangle\langle b_0|, |a_j\rangle\langle a_j|]$$

$$\propto -\frac{1}{M}(|a_l\rangle\langle a_j| + |a_j\rangle\langle a_l|). \tag{10}$$

We construct the remaining $M(M-1)/2$ off-diagonal generators by considering

$$\frac{1}{M}[|a_l\rangle\langle a_j| + |a_j\rangle\langle a_l|, |a_l\rangle\langle a_l|]$$

$$= \frac{1}{M}(i|a_j\rangle\langle a_l| - i|a_l\rangle\langle a_j|). \tag{11}$$

The generators synthesized in Eqs. (10) and (11) are precisely the off-diagonal beam-splitter generators that are not typically accessible in spin-wave quantum memories. Note that we have only used the $|b_0\rangle$ momentum-space phase shift. However, the off-diagonal elements are reduced by a factor of $1/M$. For

this reason, although the $\hat{H}_0^k \sim |b_0\rangle\langle b_0|$ phase shift generator is sufficient for controllability, the beam-splitter interactions become weaker as the system size M grows. Accomplishing arbitrary unitary dynamics would require pulse sequences that grow unfavorably with M. Next, we present a different Hamiltonian generator that allows us to implement spin-wave beam splitters in a single ensemble that alleviates this deleterious scaling, showing that arbitrary two-mode beam splitters can be implemented in constant time, even in the large-M limit.

B. Numerically optimized beam splitters

Since controllability is possible without two ensembles in principle, it is worthwhile to describe a construction that achieves efficient linear controllability in a single ensemble. Unlike in the previous section, we will work here in the momentum basis $|b_k\rangle$. A beam splitter between spin-wave modes $\hat{b}_j$ and $\hat{b}_l$ can be generated by the Hamiltonian

$$\hat{H}_{jl}^{BS} \propto (|b_j\rangle + |b_l\rangle)(\langle b_j| + \langle b_l|), \quad (12)$$

with $j \neq l$. Expanding out the state $|b_j\rangle + |b_l\rangle$ shows that this Hamiltonian corresponds to both phase modulation and amplitude modulation across the spin wave:

$$|b_j\rangle + |b_l\rangle = \frac{1}{\sqrt{M}} \sum_{x=0}^{M-1} (e^{2\pi i jx/M} + e^{2\pi i lx/M}) |a_x\rangle \quad (13)$$

due to the summation of the complex amplitudes at each site. For this reason, we are not able to apply this Hamiltonian directly using only phase shifts. This is one reason that previous experiments have not achieved complete controllability in a spin-wave register.

In order to overcome this challenge, we propose to implement a similar Hamiltonian that is generated using only phase shifts but nonetheless yields efficient unitary controllability. The modified Hamiltonian is

$$\hat{H}_{jl}' \propto |b'\rangle\langle b'|, \quad (14)$$

$$|b'\rangle = \frac{1}{\sqrt{M}} \sum_{x=0}^{M-1} \exp[i \arg(e^{2\pi i jx/M} + e^{2\pi i lx/M})] |a_x\rangle. \quad (15)$$

$\hat{H}_{jl}'$ only applies the phase component of the beam-splitter Hamiltonian $\hat{H}_{jl}^{BS}$. This Hamiltonian may be constructed using only phase shifts, by turning on the cavity coupling Hamiltonian $\hat{H}_0^k$ [Eq. (7)] to a spin-wave state with the nontrivial phase $\arg(e^{2\pi i jx/M} + e^{2\pi i lx/M})$, instead of the $k = 0$ mode. Experimentally, this would be done in a two-step process, first applying the phase modulation and then turning on the cavity coupling. The modified beam-splitter Hamiltonian $\hat{H}_{jl}'$ does not generate an exact two-mode beam splitter on its own. However, using $\hat{H}_{jl}'$ in conjunction with the two other available Hamiltonians $\hat{H}_j \propto |b_j\rangle\langle b_j|$ and $\hat{H}_l \propto |b_l\rangle\langle b_l|$ in a multipulse sequence allows us to do so. Next, we present the procedure to numerically and analytically generate a precise two-mode beam splitter using $\hat{H}_{jl}'$.

The three operators $\hat{H}_{jl}'$, $\hat{H}_j$, and $\hat{H}_l$ define a three-level system with basis states $|b_j\rangle$, $|b_l\rangle$, and $|b^*\rangle$. $|b^*\rangle$ is defined
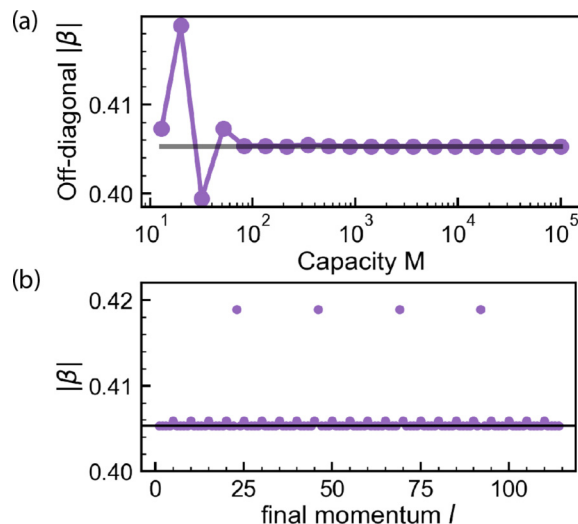
FIG. 4. Beam splitters with a single ensemble. (a) The off-diagonal matrix element β is plotted for the optimized momentum-space beam splitter $\hat{H}_{jl}'$. β remains large for all values of M, indicating an effective beam splitter, and approaches a constant value $4/\pi^2$ for large M (solid gray line). (b) β is plotted for $M = 115$ and $j = 0$ vs l, indicating that beam splitters are possible for all values of $l - j$. Slight variation in β is observed for values of $l - j$ that are multiples of a large divisor of M, evident in the plot for values of l that are multiples of 5 and 23.

so that $|b^*\rangle$, $|b_l\rangle$, and $|b_j\rangle$ form an orthonormal basis of the three-dimensional space spanned by $|b'\rangle$, $|b_j\rangle$, and $|b_l\rangle$. To construct $|b^*\rangle$, we subtract from $|b'\rangle$ its projections on $|b_j\rangle$ and $|b_l\rangle$ and normalize the result.

Efficiently generating a beam splitter requires the generating Hamiltonian $\hat{H}_{jl}'$ to have large off-diagonal element $\beta = \langle b_l| \hat{H}_{jl}' |b_j\rangle$. We write $\hat{H}_{jl}'$ in the basis $(|b_j\rangle, |b_l\rangle, |b^*\rangle)$:

$$\hat{H}_{lj}' = \begin{pmatrix} \alpha & \beta^* & \gamma^* \\ \beta & \epsilon & \zeta^* \\ \gamma & \zeta & \theta \end{pmatrix}. \quad (16)$$

The element β describes the beam-splitter strength. In Fig. 4(a), we plot the magnitude of β for the $\hat{H}_{jl}'$ Hamiltonian (purple) as a function of M for $j = 1$ and $l = 8$. This plot shows that $\hat{H}_{jl}'$ can be used to generate an effective beam splitter at large M, since β remains at a value of nearly 0.4. Figure 4(b) displays the magnitude of β for $M = 115$ as a function of l for $j = 1$. The exact values of the elements of $\hat{H}_{jl}'$ depend on j, l, and M, but critically, they remain large for all values and approach the value of $4/\pi^2$ for large M, shown as a solid dark line in Figs. 4(a) and 4(b). The resulting value of $4/\pi^2$ is derived by calculating $\langle b_l|b'\rangle$ (or, equivalently, $\langle b_j|b'\rangle$) for large M. For values where $l - j$ are a multiple of a large divisor of M, departures from the nominal value $\beta = 4/\pi^2$ are observed. For example, small deviations at multiples of 5 and 23 can be observed in Fig. 4 for $M = 115$ where 23 and 5 are the only nontrivial divisors of 115. In cases such as this, the exact Hamiltonian that depends on l and j may be calculated from Eqs. (12) and (13).

TABLE I. Approximate numeric rotation angles for each unitary of the optimized 50-50 beam splitter in Eq. (19).

i	$\theta_i/2\pi$
1	0.347136
2	0.222136
3	0.222136
4	0.125
5	0.652864
6	0.652864
7	0.777864

For large M, when the value of $l - j$ is not related to a large integer divisor of M, the Hamiltonian $\hat{H}'_{lj}$ becomes

$$
\hat{H}'_{lj} = \begin{pmatrix}
4/\pi^2 & 4/\pi^2 & \sqrt{\frac{4}{\pi^2}\left(1 - \frac{8}{\pi^2}\right)} \\
4/\pi^2 & 4/\pi^2 & \sqrt{\frac{4}{\pi^2}\left(1 - \frac{8}{\pi^2}\right)} \\
\sqrt{\frac{4}{\pi^2}\left(1 - \frac{8}{\pi^2}\right)} & \sqrt{\frac{4}{\pi^2}\left(1 - \frac{8}{\pi^2}\right)} & 1 - \frac{8}{\pi^2}
\end{pmatrix}.
$$

(17)

Importantly, in the large-M limit, $\hat{H}'_{lj}$ becomes independent of l, j, and M.

To generate exact beam splitters, we numerically optimize amplitudes in an interleaved pulse sequence. The desired 50-50 beam-splitter unitary is

$$
\hat{U}^{\mathrm{BS}} = \frac{1}{\sqrt{2}} \begin{pmatrix}
1 & i & 0 \\
i & 1 & 0 \\
0 & 0 & \sqrt{2}
\end{pmatrix}.
$$

(18)

For large M, we find that $\hat{U}^{\mathrm{BS}}$ can be achieved in a seven-pulse sequence of the form

$$
\hat{U}^{\mathrm{BS}} = \hat{U}'_{lj}(\theta_7) \cdot \hat{U}_l(\theta_6) \cdot \hat{U}_j(\theta_5)
$$
$$
\cdot \hat{U}'_{lj}(\theta_4) \cdot \hat{U}_l(\theta_3) \cdot \hat{U}_j(\theta_2) \cdot \hat{U}'_{lj}(\theta_1),
$$

(19)

where each unitary is derived from its respective Hamiltonian: $\hat{U}_l(\theta) = e^{-i\hat{H}_l\theta}$, $\hat{U}_j(\theta) = e^{-i\hat{H}_j\theta}$, and $\hat{U}'_{lj}(\theta) = e^{-i\hat{H}'_{lj}\theta}$. The solutions for the rotation angles $\{\theta_1, \ldots, \theta_7\}$ are given analytically in the Supplemental Material [52]. The approximate numerical values are shown in Table I. For large M, this solution is valid for arbitrary values of j and l as long as $l - j$ is not a multiple of a large integer divisor of M.

The key achievement of this construction is that exact two-mode beam splitters may be achieved between any two spin-wave modes in constant (independent of M) time, even for large M. This type of connectivity is unique relative to most optical setups where usually only two-mode beam splitters operating between adjacent modes are implemented. In the future, other useful beam-splitter constructions may be obtained by considering phase-modulation theory, using phase modulation and single-mode phase shifts to create arbitrary unitary operations. Investigations into other experimentally convenient tools for linear control will remain an area for further research.

V. OPERATIONAL FIDELITY

We now assess the operational fidelities of our proposal due to various sources of error. First, we calculate the size of fundamental sources of error present in the atomic spin-wave processor. These errors, present for any implementation using optical qubits in a cavity, arise from atomic saturation and atomic emission into the cavity and into free space. Next, in Sec. V B, we discuss additional technical sources of error that will likely arise in the cold-atom implementation.

A. Fundamental beam-splitter errors

In this section, we briefly discuss the scale of fundamental errors that arise in the beam-splitter operation $\hat{H}^{\mathrm{BS}}$,

$$
\hat{H}^{\mathrm{BS}} = -\hbar \frac{\Omega^2}{4\delta} \left(\hat{b}_0^{\dagger A} + \hat{b}_0^{\dagger B} \right)\left(\hat{b}_0^A + \hat{b}_0^B \right).
$$

(20)

Three sources of error are considered: atomic saturation (Sec. V A 1), free-space emission (Sec. V A 2), and cavity emission (Sec. V A 3).

1. Atomic saturation

Atomic saturation induces error in a spin-wave beam splitter through the introduction of anharmonicity that leads to deviations from a linear beam splitter. The scaling of this error can be derived from the Holstein-Primakoff transformation [46], $\hat{J}_+ = \sqrt{N}\hat{b}_0^\dagger \sqrt{1 - \frac{\hat{b}_0^\dagger \hat{b}_0}{N}}$, $\hat{J}_- = \sqrt{N}\sqrt{1 - \frac{\hat{b}_0^\dagger \hat{b}_0}{N}}\hat{b}_0$. The atom-cavity Hamiltonian of Eq. (7) can then be written as

$$
\hat{H}_0^k \propto \hat{b}_0^\dagger \hat{b}_0 - \frac{\hat{b}_0^\dagger \hat{b}_0^\dagger \hat{b}_0 \hat{b}_0}{N}.
$$

(21)

If we assume that mode $\hat{b}_0$ is occupied by m excitations, the relative size of the second term (the error) of this Hamiltonian scales as m/N. This Hamiltonian leads to the following equation of motion describing $\hat{b}_0$:

$$
\dot{\hat{b}}_0 \propto i \left(\hat{b}_0 - \frac{2}{N} \hat{b}_0^\dagger \hat{b}_0 \hat{b}_0 \right).
$$

(22)

The second (error) term in Eq. (22) leads to an erroneous phase accumulation in $\hat{b}$ of magnitude $2(m-1)/N$, which leads to a beam-splitter error (1 minus fidelity) of $E_M \sim (m-1)^2/N^2$. For the unitary beam splitters and phase shifts we consider here, the loss in fidelity due to anharmonicity always scales quadratically since the error is being expanded around a minimum. For Fig. 5 (see Sec. V A 4), we assume the worst-case scenario for the anharmonicity error, by assuming that m scales linearly with the mode capacity M, $m \propto M$.

In the future, it may be possible to devise a spin-wave quantum computing scheme that can operate outside of the linear regime and avoid this error. In this paper, we choose to treat anharmonicity as an error that negatively affects the figure of merit of the spin-wave processor in Fig. 5.

2. Free-space emission

We now consider errors due to free-space emission while the atom-cavity coupling is turned on for the duration of a beam-splitter operation. Atoms emit into free space with probability $P = \Gamma_2 T$, where the beam splitter is applied for
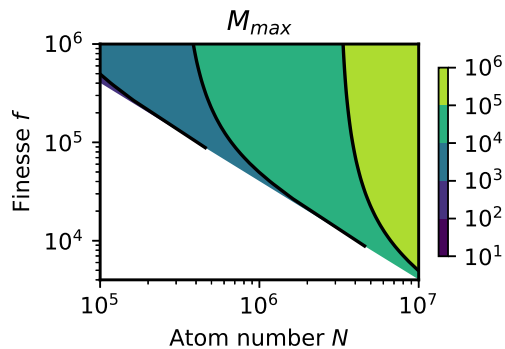
FIG. 5. Maximum processor capacity $M_{\max}$ vs finesse f and total atom number N. $M_{\max}$ is defined as the maximal capacity M that leads to a beam-splitter error of less than 10^{-3} for a single-atom cooperativity of $C = 10^{-4}f$.

a time $T \sim \delta/\Omega^2$, leading to an error

$$E_{\text{FS}} \sim \frac{\Gamma \delta}{\Omega^2}. \tag{23}$$

This error scales as the ratio of the loss rate Γ and the strength of the Hamiltonian in Eq. (7). This error decreases for smaller detunings δ.

3. Cavity emission error

Next, we calculate the error that results from atoms emitting into the cavity mode during a beam-splitter operation. For a far-detuned cavity, the emission rate Γ_c into the cavity mode is

$$\Gamma_c \sim \kappa \frac{\Omega^2}{\delta^2}, \tag{24}$$

where κ is the cavity decay rate and $\frac{\Omega^2}{\delta^2}$ represents the intracavity photon number. The resulting error E_c is of order $\Gamma_c T$ with the beam splitter being applied for $T \sim \delta/\Omega^2$, leading to

$$E_c \sim \Gamma_c T \sim \frac{\kappa}{\delta}. \tag{25}$$

This error improves with larger detunings δ, which may be increased up to the cavity free spectral range (FSR): $\delta_{\max} \sim$ FSR. Therefore the smallest fractional error in a beam splitter or collective phase shift reduces to $E_c \sim 1/f$ for an optical cavity with finesse f. However, the optimum detuning is one that sets E_{FS} and E_c equal. Optimal detunings such as this are common in atom-cavity processes [53]. In this case, the optimum is

$$\delta_{\text{opt}} \sim \Omega \sqrt{\frac{\kappa}{\Gamma}} = \sqrt{NC}\kappa. \tag{26}$$

At the optimum detuning, the errors are

$$E_{\text{FS}} \sim E_c \sim 1/\sqrt{NC}. \tag{27}$$

These errors are summed to evaluate the maximum capacity in Fig. 5.

4. Capacity limits due to fundamental errors

The beam-splitter errors are dependent on the total spin-wave processor capacity M. We now calculate the maximum capacity M that can be achieved while maintaining a single beam-splitter error of less than 10^{-3}.

The total error $E = E_M + E_{\text{FS}} + E_c$ is optimized (minimized) at a detuning $\delta_{\text{opt}} = \kappa\sqrt{NC}$, where $E_{\text{FS}} \sim E_c \sim 1/\sqrt{NC}$. In Fig. 5, we plot the maximum capacity $M_{\max}$ at which the total error E is less than 10^{-3} for a cavity with single-atom cooperativity $C = 10^{-4}f$ and finesse f. In the white region of the plot, the error E is above 10^{-3} even for $M = 1$. This region corresponds to $2/\sqrt{NC} > 10^{-3}$. Since the maximum possible detuning is given by the free spectral range (FSR) $\delta \sim$ FSR $= \kappa f$, large finesse $f > 10^3$ is also required to achieve $E < 10^{-3}$. Importantly, for less-than-state-of-the-art experimental values of $N \sim 5 \times 10^5$ and $f \sim 5 \times 10^5$, the error is $E < 10^{-3}$ even with a capacity of over $M = 10^3$. For larger atom numbers, $M_{\max} > 10^4$ is possible. Current atom-cavity experiments used to generate large amounts of atomic spin squeezing [54,55] commonly operate with $NC > 10^5$, a value that would already access errors below 1%.

B. Technical sources of error

1. Effect of momentum displacement errors

First we consider the effect of small-amplitude errors in the momentum displacement operator $\hat{\Delta}$. This operator works correctly when the amount of phase shift leads to an integer change in the momentum index. We consider the effect of small imperfections ϵ in the amplitude of this operation, which results in a noninteger momentum $k \to k + 1 + \epsilon$. The error η_Δ is calculated to be

$$\eta_\Delta = 1 - |\langle b_{k+\epsilon}|b_k\rangle|^2$$

$$= 1 - \left|\frac{1}{M}\sum_{j=1}^{M} e^{2\pi i \epsilon j/M}\right|^2$$

$$\approx \pi^2\epsilon^2, \tag{28}$$

in the limit of small ϵ and large M. The loss of quantum fidelity is second order in the error ϵ. However, nonetheless, the $\hat{\Delta}$ operation will require good amplitude control. More complex pulse sequences that are amplitude independent to higher order—similar to those used in nonlinear magneto-optical rotation (NMOR), pulsed spectroscopy, dynamic decoupling, and optimal control [56–58]—may be useful to eliminate this error in experimental settings.

2. Errors from variation in atom number

The goal of this apparatus will be to achieve an approximately constant atom number per site, N/M. However, some variation will likely remain. We estimate the errors from this variation. In the case of nonuniform atom number per site, the cavity dressing interaction is rewritten using a nonuniform projector $|b_0'\rangle$

$$H_0^{k*} = \frac{\hbar\Omega_2^2}{4\delta_2}|b_0'\rangle\langle b_0'|, \tag{29}$$

$$|b_0'\rangle = \sum_{j=0}^{M-1}\sqrt{\frac{n_j'}{N}}|a_j\rangle, \tag{30}$$

$$|a_j\rangle = \frac{1}{\sqrt{n_j'}}\sum_{l=0}^{n_j'-1}|g_l\rangle\langle e_l|, \tag{31}$$

where $n'_j = n(1 + \epsilon_j)$ is the erroneous factor describing the nonuniform atom number at site j and the errors ϵ_j are assumed to sum to zero. With atom-number variation, this cavity coupling Hamiltonian is not equivalent to $H_0^k \propto |b_0\rangle\langle b_0|$. The cavity interaction leads to a phase shift in a new mode $|b'_0\rangle$, a mode that is not trivially decomposable into the orthogonal basis. Assuming that the orthogonal basis must be maintained for the desired operations, this leads to an error of

$$\eta_N = 1 - |\langle b_0|b'_0\rangle|^2 \approx \frac{1}{M}\sum_{j=0}^{M-1}\frac{\epsilon_j^2}{4} \tag{32}$$

for small errors ϵ_j. η_N will likely be dominated by static inhomogeneities in atom number and shot-to-shot fluctuations. Well-designed atom loading techniques and real-time feedback can be used to reduce atom-number fluctuations and inhomogeneities below 1% [55], but dealing with nonuniform ensembles may require additional work in the future.

Additional static errors may arise as well, for example, due to the nonzero extent of each array site or inhomogeneous coupling of the atoms to the cavity due to the radial and axial extent. These errors follow the scaling of Eq. (32), and initial estimates indicate that these errors will also be small. Importantly, decoherence errors due to nonzero array site width do not grow with capacity. However, overall, further technical improvements will be needed to mitigate technical sources of error as they are encountered. Static errors, such as the ones mentioned in this section, may be corrected using compensation techniques in the pulses or perhaps appropriate redefinition of the basis.

C. Initialization time

Initialization of single-photon excitations in the spin-wave memory may be achieved by several different methods. Here, we consider probabilistically creating, in rapid succession, single excitations in a large array of momentum eigenstates. The level diagram for this write process is shown in the inset of Fig. 6(b). The level scheme is the inverse of the diagram in Fig. 1 and requires one additional longitudinal cavity mode, which can easily be selected with the frequency of the initialization laser (also called the write laser). The initialization laser must counterpropagate relative to the dressing laser to maintain phase matching of both the read and write photons into the cavity mode [37].

Memory initialization is accomplished using the standard atomic memory heralded write process into the $|b_0\rangle$ mode [59], followed by a unit displacement $\hat{\Delta}$, repeated until a large fraction of the spin-wave modes are initialized. It is important to keep the probability of double excitation low, since such errors are not detected by heralding. In atomic memories, the double-excitation error η_2 is proportional to the write probability p_1, $\eta_2 \propto p_1$, meaning that the write probability must be kept small [60]. However, when excitations are initialized within an M-mode register, the standard double-excitation error η_2 due to atomic emission into free space is amplified. Normally, the full error from the write process η_w is of scale η_2 [60]. However, in an M-mode spin-wave register, each mode gains an independent error of scale η_2 for every write
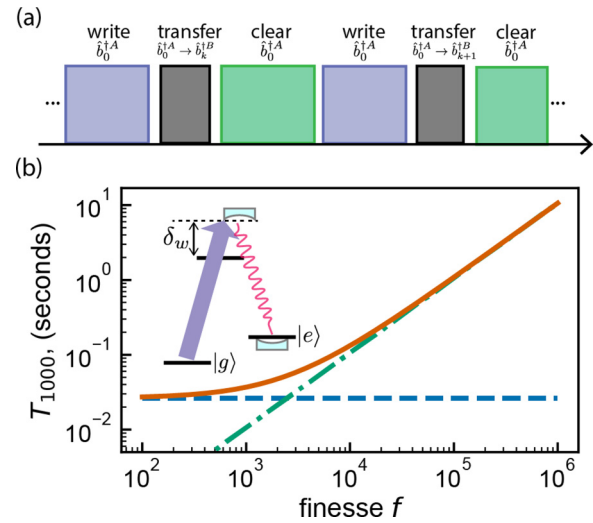
FIG. 6. (a) Initialization sequence. Excitations are written into ensemble A and transferred to ensemble B to prevent compounding errors. (b) Approximate initialization time for 1000 single-photon excitations in the ensemble for a 2-cm-length optical cavity. The initialization time is limited by both the cavity lifetime [green dot-dashed line, given by $1000/(\eta_w\kappa)$] and atomic excited state lifetime [blue dashed line, given by $1000/(\eta_w\Gamma)$] with the total time shown in orange (solid curve). The level diagram for memory initialization is shown in the inset.

process, so that the total error in each mode compounds to a larger value $\eta_w \sim M\eta_2$.

In order to overcome this unfortunate scaling and recover the original scaling $\eta_w \sim \eta_2$, we propose a modified heralded initialization scheme that works in the two-ensemble configuration. The pulse sequence is displayed in Fig. 6(a). By writing excitations into a single ensemble (chosen to be mode $\hat{b}_0^A$ here), the excitation can be initialized and transferred with a low-error beam-splitter operation into ensemble B. Ensemble A can be cleared with a standard optical pumping pulse (labeled "clear"), before subsequent excitations are written. The optical pumping prevents errors in the initial write procedure from compounding in later steps.

In Fig. 6(b), we plot the approximate initialization time required to initialize 1000 modes. The speed limits for the memory write process are dictated by the excited state linewidth Γ and the cavity linewidth κ. Using these rates, and maintaining a single write error $\eta_w \sim \eta_2 \sim p_1$ of less than 0.001, we plot the estimated time T_{1000} required to create 1000 single excitations in Fig. 6 versus cavity finesse f:

$$T_{1000} \sim \frac{1000}{\eta_w}\left(\frac{1}{\Gamma} + \frac{1}{\kappa}\right). \tag{33}$$

The cavity linewidth κ is related to finesse by $\kappa = 2\pi c/(lf)$, where c is the speed of light and l is the round-trip cavity length. We see that the cavity lifetime becomes the limiting factor at a finesse of around 2000, for a cavity length of 2 cm, assuming ideal detection efficiency. Although the initialization time for 1000 excitations and $f = 10^4$ is still well below the maximum atomic lifetimes observed in spin-wave memories [45], this speed limit may be a significant concern for future high-capacity memories in high-finesse cavities.

Deterministic initialization methods involving single photon sources or Rydberg excitations are also possible and eliminate the speed bottleneck. Such schemes have already been demonstrated in a laboratory setting [61,62].

D. Readout

Another important ingredient for the spin-wave quantum processor is readout. Readout is required for almost all photonic processes and is necessary for linear optical quantum computing. The readout process is not a focus of this paper, because spin-wave readout has been studied in depth in many previous quantum memory experiments [3,12,63]. In particular, atom-cavity systems demonstrate the most efficient readout of any type of quantum memory with intrinsic readout probabilities of well over 90% possible [3]. Many effective quantum networking protocols are stable to inefficiencies at this level [60]. In scenarios when many spin-wave modes need to be read out in succession, compounding errors may arise, equivalently to the initialization process. In this case, a readout transfer method, equivalent to that of Fig. 6(a), may be used.

E. Technical challenges

Additional technical challenges will likely arise when building an experiment to accomplish this proposal. The application of the Raman dressing laser results in a shift in the cavity resonance frequency by amount $\Delta\omega_c \approx N_g g^2/\delta_1$ and a shift in the two-photon resonance frequency ω_{eg} by amount $\Delta\omega_{eg} \approx \Omega_d^2/\delta_1$. These shifts will need to be taken into account to achieve accurate dynamics in the two-photon system. To achieve effective operations, the laser detunings may need to be actively stabilized to account for these cavity and state shifts, as has been done in recent entanglement-generation experiments [54,55].

Rapidly addressing a large capacity of quantum bits or modes is a ubiquitous challenge in nearly every experimental quantum platform. Here, we achieve that end simply, using a single optical cavity mode and an off-resonant light source. One advantage of the proposal is that the $\hat{\Delta}$ operator can be implemented with light that is at a frequency far from atomic resonance, with no stringent wavelength or power requirements. We envision a fast electro-optic system operating in the near infrared, which can operate with switching ranges of well over 1 GHz.

Overall, we are optimistic that holographic spin-wave excitations in a cavity-coupled ensemble may become a useful platform for quantum information processing. The system combines several attractive characteristics including efficient readout into a single optical cavity mode, large capacity, and universal processing capabilities able to achieve high fidelity. In the long term, many quantum information processing devices will likely require networked operation, and atom-cavity systems will be an architecture to achieve this.

VI. SQUEEZING AND CONTINUOUS-VARIABLE PROCESSING

Atom-cavity experiments have recently generated record amounts of squeezing, entanglement useful for enhancing quantum sensors [54,55]. Squeezing of 20 dB, or a factor 100 in variance, is now achievable in systems similar to the one proposed here. Additionally, recent optical experiments have shown how to use squeezing as a powerful computational resource to create dual-rail cluster states [64]. Cluster states are particularly appealing for future quantum processors because they are deterministic and are amenable to powerful continuous-variable quantum error correction schemes [25,65]. By creating an M-mode processor, we now open the possibility to combine the cluster state concept with large amounts of atomic spin squeezing to build a continuous-variable atomic processor. Here, we describe how to implement the optical dual-rail cluster state scheme in the atom-cavity system. The cold-atom system leads to numerous advantages relative to the photonic implementation since the qubits are stationary and amenable to feedback and high-fidelity processing with no losses.

There are several viable paths to create spin squeezing in the spin-wave memory including one- and two-axis twisting and quantum nondemolition (QND) measurements. For example, the squeezing operation may be described by an operator $\hat{S}(\alpha) = \exp[\frac{1}{2}(\alpha\hat{b}_0^2 - \alpha\hat{b}_0^{\dagger 2})]$ that squeezes only the $k = 0$ mode. In this case, the mode operators are transformed as

$$\hat{b}_0 \to \hat{S}^{\dagger}(\alpha)\hat{b}_0\hat{S}(\alpha) = \hat{b}_0 \cosh(\alpha) - \hat{b}_0^{\dagger} \sinh(\alpha), \quad (34)$$

$$\hat{b}_k \to \hat{S}^{\dagger}(\alpha)\hat{b}_k\hat{S}(\alpha) = \hat{b}_k \quad (k \neq 0). \quad (35)$$

Critically, the operator $\hat{S}$ does not affect modes $\hat{b}_k$ with $k \neq 0$, which are orthogonal to $\hat{b}_0$. This operation allows us to create independently squeezed spin-wave modes. In the next section, we present a description of how to create an M-mode squeezed state where each k mode is spin squeezed. This state, when passed through $2M - 1$ beam splitters, transforms into a dual-rail cluster state that may be used for universal quantum computation. This method is a direct adaptation of seminal results in the optical regime, creating continuous-variable cluster states of light [66].

A. Cluster state generation

Spin-wave continuous-variable quantum computing can be achieved using the same basis as linear optical spin-wave computing. We consider a similar protocol to experiments in the optical regime that have generated dual-rail cluster states with over 10 000 nodes [66].

A continuous-variable cluster state is a large entangled state defined by nullifiers, analogous to the stabilizers of a discrete cluster state [23]. The nullifiers are joint operators that describe noise projection of nearest-neighbor spin waves. The nullifiers in our spin-wave case are

$$\epsilon_k^x = \hat{\mathcal{X}}_k^A + \hat{\mathcal{X}}_k^B + \hat{\mathcal{X}}_{k+1}^A - \hat{\mathcal{X}}_{k+1}^B, \quad (36)$$

$$\epsilon_k^p = \hat{\mathcal{P}}_k^A + \hat{\mathcal{P}}_k^B - \hat{\mathcal{P}}_{k+1}^A + \hat{\mathcal{P}}_{k+1}^B, \quad (37)$$

for any mode k (modulo M), where $\hat{\mathcal{X}}_k^A$ and $\hat{\mathcal{P}}_k^A$ are the quadrature operators for the $\hat{b}_k^A$ spin wave. Optical experiments have achieved entanglement, as detected by a reduction in $|\langle\epsilon^x\rangle|^2$ and $|\langle\epsilon^p\rangle|^2$ below a value of 1/2. Current demonstrations
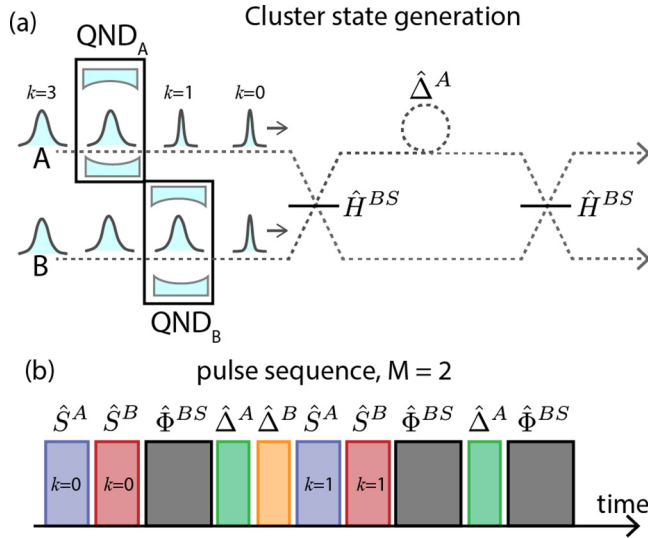
FIG. 7. Cluster state generation scheme. (a) Optical diagram for generating a spin-wave cluster state. QND measurements are sequentially applied to squeeze each momentum state. Using two beam splitters and a phase shift $\hat{\Delta}^A$, a dual-rail cluster state is created. Additional unshown momentum shift operators $\hat{\Delta}^A$ and $\hat{\Delta}^B$ are necessary to transfer spin waves in and out of the $k = 0$ interaction mode. (b) Example pulse sequence for generating a dual-rail cluster state with $M = 2$. Pulse colors are set to match Fig. 1, and the squeezing pulses are labeled with the affected initial value of k.

FIG. 8. Capacity M of a spin-wave cluster that can achieve 20 dB of spin squeezing simultaneously in each mode ($S_M = 100$) as a function of the atom number N and squeezing R_s, the quantum noise reduction in each mode. M is optimized at $R_s = eS_M$ (pink line).

have reached values of around -6 dB [66]. State-of-the-art spin squeezing may be able to reduce these quadrature values to -20 dB or smaller, potentially reaching the fault-tolerant threshold for Gottesman-Kitaev-Preskill (GKP)-type quantum error correction [25,67].

An experimental diagram is shown in Fig. 7. Two ensembles (labeled "A" and "B") are loaded into the bow-tie cavity, one on each side. The ensembles each provide a basis of momentum states $|b_k^A\rangle$ and $|b_k^B\rangle$ for $0 \leqslant k < M$. The goal is to use collective cavity quantum nondemolition (QND) measurement or another technique [54,55] to generate spin squeezing in each momentum mode, and then use collective cavity interactions to emulate the beam splitters required to transform the squeezed modes into a cluster state.

First, cavity QND measurements or other squeezing operations $\hat{S}$ are performed on each individual spin wave to create a stream of squeezed states. Spin waves are transferred into and out of cavity coupling with the $\hat{\Delta}^A$ and $\hat{\Delta}^B$ operators. Using the well-known construction for creating dual-rail cluster states [66], two-mode beam splitters $\hat{H}^{\mathrm{BS}}$ and phase shifts $\hat{\Delta}^A$ and $\hat{\Delta}^B$ are sufficient for creation. Unlike optical cluster states, the atomic dual-rail cluster state is stationary with long coherence time, and hence amenable to real-time computation.

In Figs. 8(a) and 8(b), we estimate the maximum capacity M of the spin-wave processor for storing a large cluster state. The amount of squeezing and the capacity will be limited by several factors, including the beam-splitter errors and the abil-

ity for the atom-cavity system to generate squeezing in the first place. However, one fundamental and dominant limitation is the capacity of the atomic system to store spin-squeezed states without a subsequent reduction in coherence due to nonlinearity (i.e., curvature of the Bloch sphere leading to nonlinear projections of the Bloch vector onto a 2D plane).

State-of-the-art atom-cavity experiments can generate spin squeezing with spectroscopic enhancement near a factor of 100 [54,55]. Spectroscopic enhancement, or the amount of squeezing, is defined as the entanglement-generated improvement in the sensor's ability to resolve a quantum phase. For a single spin wave, we write the spectroscopic enhancement [53]

$$S_s = R_s \mathcal{C}^2, \tag{38}$$

where $R_s^{-1} = 2 \operatorname{Var}(\hat{J}_z)/N$ is the reduction in variance of the expectation value of the collective spin operator $\hat{J}$ along a particular axis (chosen as z here). We choose R_s to be the inverse of noise reduction so that it scales proportionally to the spectroscopic enhancement S_s. $\mathcal{C}$ is the spin coherence of the ensemble defined as $\mathcal{C} = J/(N/2)$, where $J \equiv \langle \hat{J} \rangle$ is the expectation value of the total projection of $\hat{J}$. J can have values between $N/2$ (full spin coherence) and 0 (no spin coherence). $S_s > 1$ is both a witness for atomic entanglement as well as a measure of the entanglement-generated improvement in the quantum sensor.

B. Multimode squeezing capacity

We now consider simultaneous equal squeezing in all M modes of an ensemble. In this case, we reduce the quantum noise in all spin-wave modes by an equal amount R_s. S_s is defined to be the squeezing that would be observed in a spin wave, if no other modes were squeezed. However, when all modes are squeezed at the same time, we observe a lower amount of squeezing in each mode, which we denote S_M. To calculate S_M, we must include the additional reduction in total $\mathcal{C}$ due to Bloch sphere curvature, which leads to a compounding reduction in squeezing in every mode. Then, the observed squeezing of a single mode in the presence of

squeezing in all other modes is

$$S_M \approx R_s \prod_{j=0}^{M-1} C_j^2, \tag{39}$$

where C_j is the spin coherence in each mode that additionally limits the total squeezing. The coherence of each mode is limited by quantum back action and the curvature of the Bloch sphere [68]. Each spin wave has a root-mean-square (rms) back action around the Bloch sphere of angle $\theta_{\rm rms} = \theta_{\rm SQL}\sqrt{R_s}$, where $\theta_{\rm SQL} = 1/\sqrt{N}$ is the standard quantum limit in radians (see, for example, Ref. [55]). This leads to a fundamental loss in coherence in each spin wave, due to Bloch sphere curvature:

$$C_j \approx e^{-\theta_{\rm rms}^2/2} \approx e^{-\theta_{\rm SQL}^2 R_s/2}. \tag{40}$$

By combining Eqs. (40) and (39), the maximum M-mode squeezing is found to be

$$S_M \approx R_s e^{-M\theta_{\rm SQL}^2 R_s}. \tag{41}$$

Quantum inefficiency and other decoherence sources that would cause further loss of coherence are not considered.

In Fig. 8, we plot the value of M that is achieved for $S_M = 100$, that is, 20 dB of squeezing versus N and R_s. The maximum capacity $M_{\rm opt}$ is found at $R_s = eS_M$. The maximized value is

$$M_{\rm opt} = \frac{N}{2eS_M}. \tag{42}$$

A processor reaching the levels of performance in Fig. 8 would be state of the art and likely useful for deterministic quantum networking and entanglement distribution. Furthermore, 20 dB of squeezing in each mode would reach or nearly reach the fault-tolerant threshold [25] for continuous-variable quantum computing.

VII. CONCLUSION

Overall, deterministic continuous-variable quantum computing has significantly better prospects for scalability than linear optics with single-quanta excitations, because the linear optics scheme requires a significant resource overhead to achieve deterministic processing [25]. However, in the near term, small-scale linear optical processing inside of a multiplexed quantum memory may be a significant boon toward realizing a quantum repeater with medium to high speed of entanglement generation over long distances (over 100 km) [11,69]. Multiplexing and high memory capacity constitute one of the key attributes that will allow repeaters to overcome the significant slowdown that results from the long path delay between repeater stations. Access to linear controllability within the memory will open up the possibility of small-scale processing and more advanced error correction. In particular, our results have shown that experiments with cavity finesse near 10^5 and large atom number are likely to achieve reasonably high fidelity computing ($F > 99\%$) with over 100 modes.

More work will be necessary, but initial calculations [70] show that multiplexed spin-wave memories offer immense promise for realistic, high-speed quantum communication. Meanwhile, in the continuous-variable scheme, the creation of spin-wave entangled states and the study of their uses for quantum sensing and networking applications should be one of the first experimental goals.

The multimode quantum processor presented here is also ideal for certain classes of quantum sensing problems that involve data distributed between multiple modes. The spin-wave processor utilizes $2M$ independent modes within the two N-atom ensembles, yielding enhanced capability for certain classes of measurements. Recent work has shown that distributed quantum sensors enable new sets of applications involving measurements of extended systems [71–74], and the spin-wave processor may extend these protocols to sensing and receiving data distributed into multiple spatial or temporal modes.

APPENDIX: ATOM-CAVITY HAMILTONIAN

In this Appendix, we derive the effective detuned atom-cavity Hamiltonian. The atom-cavity system is governed by the Tavis-Cummings Hamiltonian

$$\hat{H}_c = \hbar\delta\hat{c}^\dagger\hat{c} + \hbar g(\hat{c}^\dagger\hat{J}_- + \hat{c}\hat{J}_+), \tag{A1}$$

where $\hat{c}$ is the cavity field operator and $\hat{J}_- = \sum_{i=0}^{N-1} |g_i\rangle\langle e_i|$ and $\hat{J}_+ = \sum_{i=0}^{N-1} |e_i\rangle\langle g_i|$ are the collective atomic lowering and raising operators. The Hamiltonian is written in the rotating frame of the atomic transition. The Heisenberg equations of motion are

$$\dot{\hat{c}} = -i\delta c - ig\hat{J}_-, \tag{A2}$$

$$\dot{\hat{J}}_- = -igN\hat{c}. \tag{A3}$$

In the limit of large detuning, $|\delta| \gg g\sqrt{N}$, we adiabatically eliminate the cavity to obtain

$$\hat{c} \approx -\frac{g}{\delta}\hat{J}_-. \tag{A4}$$

Inserting this into Eq. (A3), we obtain

$$\dot{\hat{J}}_- = i\frac{g^2}{\delta}N\hat{J}_-, \tag{A5}$$

which can be generated by an effective Hamiltonian

$$\hat{H}_0^k = -\hbar \frac{g^2}{\delta} \hat{J}_+ \hat{J}_-. \tag{A6}$$

If the number of excitations is low, the atomic raising and lowering operators may be approximated as harmonic creation

and annihilation operators, giving rise to

$$\hat{H}_0^k = -\hbar \frac{\Omega^2}{4\delta} \hat{b}_0^\dagger \hat{b}_0, \tag{A7}$$

where $\hat{b}_0 \approx \hat{J}_-/\sqrt{N}$ and $\Omega = 2g\sqrt{N}$ is the vacuum Rabi splitting.

---

[1] K. Baumann, C. Guerlin, F. Brennecke, and T. Esslinger, Dicke quantum phase transition with a superfluid gas in an optical cavity, Nature (London) **464**, 1301 (2010).

[2] L. W. Clark, N. Schine, C. Baum, N. Jia, and J. Simon, Observation of Laughlin states made of light, Nature (London) **582**, 41 (2020).

[3] S.-J. Yang, X.-J. Wang, X.-H. Bao, and J.-W. Pan, An efficient quantum light–matter interface with sub-second lifetime, Nat. Photonics **10**, 381 (2016).

[4] B. K. Malia, J. Martínez-Rincón, Y. Wu, O. Hosten, and M. A. Kasevich, Free Space Ramsey Spectroscopy in Rubidium with Noise below the Quantum Projection Limit, Phys. Rev. Lett. **125**, 043202 (2020).

[5] E. Pedrozo-Peñafiel, S. Colombo, C. Shu, A. F. Adiyatullin, Z. Li, E. Mendez, B. Braverman, A. Kawasaki, D. Akamatsu, Y. Xiao, and V. Vuletić, Entanglement-enhanced optical atomic clock, Nature (London) **588**, 414 (2020).

[6] G. Pagano, A. Bapat, P. Becker, K. S. Collins, A. De, P. W. Hess, H. B. Kaplan, A. Kyprianidis, W. L. Tan, C. Baldwin, L. T. Brady, A. Deshpande, F. Liu, S. Jordan, A. V. Gorshkov, and C. Monroe, Quantum approximate optimization of the long-range Ising model with a trapped-ion quantum simulator, Proc. Natl. Acad. Sci. USA **117**, 25396 (2020).

[7] M. P. Harrigan, K. J. Sung, M. Neeley, K. J. Satzinger, F. Arute, K. Arya, J. Atalaya, J. C. Bardin, R. Barends, S. Boixo, M. Broughton, B. B. Buckley, D. A. Buell, B. Burkett, N. Bushnell, Y. Chen, Z. Chen, B. Chiaro, R. Collins, W. Courtney *et al.*, Quantum approximate optimization of non-planar graph problems on a planar superconducting processor, Nat. Phys. **17**, 332 (2021).

[8] I. S. Madjarov, J. P. Covey, A. L. Shaw, J. Choi, A. Kale, A. Cooper, H. Pichler, V. Schkolnik, J. R. Williams, and M. Endres, High-fidelity entanglement and detection of alkaline-earth Rydberg atoms, Nat. Phys. **16**, 857 (2020).

[9] J. H. Wesenberg, A. Ardavan, G. A. D. Briggs, J. J. L. Morton, R. J. Schoelkopf, D. I. Schuster, and K. Mølmer, Quantum Computing with an Electron Spin Ensemble, Phys. Rev. Lett. **103**, 070502 (2009).

[10] D. V. Vasilyev, I. V. Sokolov, and E. S. Polzik, Quantum volume hologram, Phys. Rev. A **81**, 020302(R) (2010).

[11] K. C. Cox, D. H. Meyer, Z. A. Castillo, F. K. Fatemi, and P. D. Kunz, Spin-Wave Multiplexed Atom-Cavity Electrodynamics, Phys. Rev. Lett. **123**, 263601 (2019).

[12] J. Simon, H. Tanji, S. Ghosh, and V. Vuletić, Single-photon bus connecting spin-wave quantum memories, Nat. Phys. **3**, 765 (2007).

[13] M. Parniak, M. Dąbrowski, M. Mazelanik, A. Leszczyński, M. Lipka, and W. Wasilewski, Wavevector multiplexed atomic quantum memory via spatially-resolved single-photon detection, Nat. Commun. **8**, 2140 (2017).

[14] P. Vernaz-Gris, K. Huang, M. Cao, A. S. Sheremet, and J. Laurat, Highly-efficient quantum memory for polarization qubits in a spatially-multiplexed cold atomic ensemble, Nat. Commun. **9**, 363 (2018).

[15] L. Heller, P. Farrera, G. Heinze, and H. de Riedmatten, Cold-Atom Temporally Multiplexed Quantum Memory with Cavity-Enhanced Noise Suppression, Phys. Rev. Lett. **124**, 210504 (2020).

[16] M. Afzelius, I. Usmani, A. Amari, B. Lauritzen, A. Walther, C. Simon, N. Sangouard, J. Minář, H. de Riedmatten, N. Gisin, and S. Kröll, Demonstration of Atomic Frequency Comb Memory for Light with Spin-Wave Storage, Phys. Rev. Lett. **104**, 040503 (2010).

[17] K. Kutluer, E. Distante, B. Casabone, S. Duranti, M. Mazzera, and H. de Riedmatten, Time Entanglement between a Photon and a Spin Wave in a Multimode Solid-State Quantum Memory, Phys. Rev. Lett. **123**, 030501 (2019).

[18] D. Lago-Rivera, S. Grandi, J. V. Rakonjac, A. Seri, and H. de Riedmatten, Telecom-heralded entanglement between multimode solid-state quantum memories, Nature (London) **594**, 37 (2021).

[19] I. Carusotto, A. A. Houck, A. J. Kollár, P. Roushan, D. I. Schuster, and J. Simon, Photonic materials in circuit quantum electrodynamics, Nat. Phys. **16**, 268 (2020).

[20] M. Saffman and T. G. Walker, Entangling single- and *N*-atom qubits for fast quantum state detection and transmission, Phys. Rev. A **72**, 042302 (2005).

[21] C. A. Muschik, I. de Vega, D. Porras, and J. I. Cirac, Quantum Processing Photonic States in Optical Lattices, Phys. Rev. Lett. **100**, 063601 (2008).

[22] A. Grankin, P. O. Guimond, D. V. Vasilyev, B. Vermersch, and P. Zoller, Free-space photonic quantum link and chiral quantum optics, Phys. Rev. A **98**, 043825 (2018).

[23] N. C. Menicucci, P. van Loock, M. Gu, C. Weedbrook, T. C. Ralph, and M. A. Nielsen, Universal Quantum Computation with Continuous-Variable Cluster States, Phys. Rev. Lett. **97**, 110501 (2006).

[24] M. Gu, C. Weedbrook, N. C. Menicucci, T. C. Ralph, and P. van Loock, Quantum computing with continuous-variable clusters, Phys. Rev. A **79**, 062318 (2009).

[25] J. E. Bourassa, R. N. Alexander, M. Vasmer, A. Patil, I. Tzitrin, T. Matsuura, D. Su, B. Q. Baragiola, S. Guha, G. Dauphinais, K. K. Sabapathy, N. C. Menicucci, and I. Dhand, Blueprint for a scalable photonic fault-tolerant quantum computer, Quantum **5**, 392 (2021).

[26] R. McConnell, H. Zhang, J. Hu, S. Ćuk, and V. Vuletić, Entanglement with negative Wigner function of almost 3,000 atoms heralded by one photon, Nature (London) **519**, 439 (2015).

[27] S. Welte, B. Hacker, S. Daiss, S. Ritter, and G. Rempe, Cavity Carving of Atomic Bell States, Phys. Rev. Lett. **118**, 210503 (2017).

[28] M. Landini, N. Dogra, K. Kroeger, L. Hruby, T. Donner, and T. Esslinger, Formation of a Spin Texture in a Quantum Gas Coupled to a Cavity, Phys. Rev. Lett. **120**, 223602 (2018).

[29] E. J. Davis, G. Bentsen, L. Homeier, T. Li, and M. H. Schleier-Smith, Photon-Mediated Spin-Exchange Dynamics of Spin-1 Atoms, Phys. Rev. Lett. **122**, 010405 (2019).

[30] Y. Guo, R. M. Kroeze, V. D. Vaidya, J. Keeling, and B. L. Lev, Sign-Changing Photon-Mediated Atom Interactions in Multimode Cavity Quantum Electrodynamics, Phys. Rev. Lett. **122**, 193601 (2019).

[31] H. Keßler, J. G. Cosme, C. Georges, L. Mathey, and A. Hemmerich, From a continuous to a discrete time crystal in a dissipative atom-cavity system, New J. Phys. **22**, 085002 (2020).

[32] S. Ostermann, W. Niedenzu, and H. Ritsch, Unraveling the Quantum Nature of Atomic Self-Ordering in a Ring Cavity, Phys. Rev. Lett. **124**, 033601 (2020).

[33] J. Nunn, K. Reim, K. C. Lee, V. O. Lorenz, B. J. Sussman, I. A. Walmsley, and D. Jaksch, Multimode Memories in Atomic Ensembles, Phys. Rev. Lett. **101**, 260502 (2008).

[34] S.-Y. Lan, A. G. Radnaev, O. A. Collins, D. N. Matsukevich, T. A. B. Kennedy, and A. Kuzmich, A multiplexed quantum memory, Opt. Express **17**, 13639 (2009).

[35] A. N. Vetlugin and I. V. Sokolov, Multivariate quantum memory as controllable delayed multi-port beamsplitter, Europhys. Lett. **113**, 64005 (2016).

[36] T.-S. Yang, Z.-Q. Zhou, Y.-L. Hua, X. Liu, Z.-F. Li, P.-Y. Li, Y. Ma, C. Liu, P.-J. Liang, X. Li, Y.-X. Xiao, J. Hu, C.-F. Li, and G.-C. Guo, Multiplexed storage and real-time manipulation based on a multiple degree-of-freedom quantum memory, Nat. Commun. **9**, 3407 (2018).

[37] J. Simon, H. Tanji, J. K. Thompson, and V. Vuletić, Interfacing Collective Atomic Excitations and Single Photons, Phys. Rev. Lett. **98**, 183601 (2007).

[38] V. Ranjan, J. O'Sullivan, E. Albertinale, B. Albanese, T. Chanelière, T. Schenkel, D. Vion, D. Esteve, E. Flurin, J. J. L. Morton, and P. Bertet, Multimode Storage of Quantum Microwave Fields in Electron Spins over 100 ms, Phys. Rev. Lett. **125**, 210505 (2020).

[39] M. Parniak, M. Mazelanik, A. Leszczyński, M. Lipka, M. Dąbrowski, and W. Wasilewski, Quantum Optics of Spin Waves through ac Stark Modulation, Phys. Rev. Lett. **122**, 063604 (2019).

[40] M. Reck, A. Zeilinger, H. J. Bernstein, and P. Bertani, Experimental realization of any discrete unitary operator, Phys. Rev. Lett. **73**, 58 (1994).

[41] N. L. R. Spong, Y. Jiao, O. D. W. Hughes, K. J. Weatherill, I. Lesanovsky, and C. S. Adams, Collectively Encoded Rydberg Qubit, Phys. Rev. Lett. **127**, 063604 (2021).

[42] W. Xu, A. V. Venkatramani, S. H. Cantú, T. Šumarac, V. Klüsener, M. D. Lukin, and V. Vuletić, Fast Preparation and Detection of a Rydberg Qubit Using Atomic Ensembles, Phys. Rev. Lett. **127**, 050501 (2021).

[43] J. Ramette, J. Sinclair, Z. Vendeiro, A. Rudelis, M. Cetina, and V. Vuletić, Any-to-any connected cavity-mediated architecture

[44] for quantum computing with trapped ions or Rydberg arrays, PRX Quantum **3**, 010344 (2022).

D. Gottesman, A. Kitaev, and J. Preskill, Encoding a qubit in an oscillator, Phys. Rev. A **64**, 012310 (2001).

[45] Y. O. Dudin, L. Li, and A. Kuzmich, Light storage on the time scale of a minute, Phys. Rev. A **87**, 031801(R) (2013).

[46] T. Holstein and H. Primakoff, Field Dependence of the Intrinsic Domain Magnetization of a Ferromagnet, Phys. Rev. **58**, 1098 (1940).

[47] M. Hosseini, G. Campbell, B. M. Sparkes, P. K. Lam, and B. C. Buchler, Unconditional room-temperature quantum memory, Nat. Phys. **7**, 794 (2011).

[48] M. Gündoğan, P. M. Ledingham, K. Kutluer, M. Mazzera, and H. de Riedmatten, Solid State Spin-Wave Quantum Memory for Time-Bin Qubits, Phys. Rev. Lett. **114**, 230501 (2015).

[49] E. Knill, R. Laflamme, and G. J. Milburn, A scheme for efficient quantum computation with linear optics, Nature (London) **409**, 46 (2001).

[50] V. Jurdjevic and H. J. Sussmann, Control systems on Lie groups, J. Differ. Equations **12**, 313 (1972).

[51] R. W. Brockett, Lie theory and control systems defined on spheres, SIAM J. Appl. Math. **25**, 213 (1973).

[52] See Supplemental Material at http://link.aps.org/supplemental/10.1103/PhysRevResearch.4.033149 for a pdf printout of a MATHEMATICA notebook that calculates the values of rotation angles $\{\theta_1, \ldots, \theta_7\}$.

[53] Z. Chen, J. G. Bohnet, J. M. Weiner, K. C. Cox, and J. K. Thompson, Cavity-aided nondemolition measurements for atom counting and spin squeezing, Phys. Rev. A **89**, 043837 (2014).

[54] O. Hosten, N. J. Engelsen, R. Krishnakumar, and M. A. Kasevich, Measurement noise 100 times lower than the quantum-projection limit using entangled atoms, Nature (London) **529**, 505 (2016).

[55] K. C. Cox, G. P. Greve, J. M. Weiner, and J. K. Thompson, Deterministic Squeezed States with Collective Measurements and Feedback, Phys. Rev. Lett. **116**, 093602 (2016).

[56] N. Khaneja, T. Reiss, C. Kehlet, T. Schulte-Herbrüggen, and S. J. Glaser, Optimal control of coupled spin dynamics: Design of NMR pulse sequences by gradient ascent algorithms, J. Magn. Reson. **172**, 296 (2005).

[57] W. Rakreungdet, J. H. Lee, K. F. Lee, B. E. Mischuck, E. Montano, and P. S. Jessen, Accurate microwave control and real-time diagnostics of neutral-atom qubits, Phys. Rev. A **79**, 022316 (2009).

[58] S. J. Glaser, U. Boscain, T. Calarco, C. P. Koch, W. Köckenberger, R. Kosloff, I. Kuprov, B. Luy, S. Schirmer, T. Schulte-Herbrüggen, D. Sugny, and F. K. Wilhelm, Training Schrödinger's cat: Quantum optimal control, Eur. Phys. J. D **69**, 279 (2015).

[59] L.-M. Duan, M. D. Lukin, J. I. Cirac, and P. Zoller, Long-distance quantum communication with atomic ensembles and linear optics, Nature (London) **414**, 413 (2001).

[60] N. Sangouard, C. Simon, H. de Riedmatten, and N. Gisin, Quantum repeaters based on atomic ensembles and linear optics, Rev. Mod. Phys. **83**, 33 (2011).

[61] L. Li and A. Kuzmich, Quantum memory with strong and controllable Rydberg-level interactions, Nat. Commun. **7**, 13618 (2016).

[62] D. P. Ornelas-Huerta, A. N. Craddock, E. A. Goldschmidt, E. A. Goldschmidt, A. J. Hachtel, Y. Wang, P. Bienias, P. Bienias, A. V. Gorshkov, A. V. Gorshkov, S. L. Rolston, and J. V. Porto, On-demand indistinguishable single photons from an efficient and pure source based on a Rydberg ensemble, Optica **7**, 813 (2020).

[63] K. S. Choi, A. Goban, S. B. Papp, S. J. van Enk, and H. J. Kimble, Entanglement of spin waves among four quantum memories, Nature (London) **468**, 412 (2010).

[64] W. Asavanant, Y. Shiozawa, S. Yokoyama, B. Charoensombutamon, H. Emura, R. N. Alexander, S. Takeda, J.-i. Yoshikawa, N. C. Menicucci, H. Yonezawa, and A. Furusawa, Generation of time-domain-multiplexed two-dimensional cluster state, Science **366**, 373 (2019).

[65] K. Fukui, A. Tomita, A. Okamoto, and K. Fujii, High-Threshold Fault-Tolerant Quantum Computation with Analog Quantum Error Correction, Phys. Rev. X **8**, 021054 (2018).

[66] S. Yokoyama, R. Ukai, S. C. Armstrong, C. Sornphiphatphong, T. Kaji, S. Suzuki, J.-i. Yoshikawa, H. Yonezawa, N. C. Menicucci, and A. Furusawa, Ultra-large-scale continuous-variable cluster states multiplexed in the time domain, Nat. Photonics **7**, 982 (2013).

[67] I. Tzitrin, J. E. Bourassa, N. C. Menicucci, and K. K. Sabapathy, Progress towards practical qubit computation using approximate Gottesman-Kitaev-Preskill codes, Phys. Rev. A **101**, 032315 (2020).

[68] A. André and M. D. Lukin, Atom correlations and spin squeezing near the Heisenberg limit: Finite-size effect and decoherence, Phys. Rev. A **65**, 053819 (2002).

[69] S. Muralidharan, L. Li, J. Kim, N. Lütkenhaus, M. D. Lukin, and L. Jiang, Optimal architectures for long distance quantum communication, Sci. Rep. **6**, 20463 (2016).

[70] P. D. Kunz, S. Santra, D. H. Meyer, Z. A. Castillo, V. S. Malinovsky, and K. C. Cox, Spatial multiplexing in a cavity-enhanced quantum memory, in *Advances in Photonics of Quantum Computing, Memory, and Communication XII*, Proceedings of SPIE Vol. 10933 (International Society for Optics and Photonics, Bellingham, WA, 2019), p. 109330P.

[71] Q. Zhuang, Z. Zhang, and J. H. Shapiro, Distributed quantum sensing using continuous-variable multipartite entanglement, in *Conference on Lasers and Electro-Optics 2018* (Optical Society of America, Washington, DC, 2018), p. FF1B.7.

[72] K. Qian, Z. Eldredge, W. Ge, G. Pagano, C. Monroe, J. V. Porto, and A. V. Gorshkov, Heisenberg-scaling measurement protocol for analytic functions with quantum sensor networks, Phys. Rev. A **100**, 042304 (2019).

[73] X. Guo, C. R. Breum, J. Borregaard, S. Izumi, M. V. Larsen, T. Gehring, M. Christandl, J. S. Neergaard-Nielsen, and U. L. Andersen, Distributed quantum sensing in a continuous-variable entangled network, Nat. Phys. **16**, 281 (2020).

[74] T. Qian, J. Bringewatt, I. Boettcher, P. Bienias, and A. V. Gorshkov, Optimal measurement of field properties with quantum sensor networks, Phys. Rev. A **103**, L030601 (2021).